IEEE Access
Multidisciplinary ⋮ Rapid Review ⋮ Open Access Journal

Received March 4, 2021, accepted March 15, 2021, date of publication March 18, 2021, date of current version April 1, 2021.

Digital Object Identifier 10.1109/ACCESS.2021.3066984

Efficient 3D Image Reconstruction of Airborne TomoSAR Based on Back Projection and Improved Adaptive ISTA

DONG HAN[1,2,3], LIANGJIANG ZHOU[1,2,3,4], ZEKUN JIAO[1,2], BINGNAN WANG[1,2,3], YACHAO WANG[1,2], AND YIRONG WU[1,2,3]

[1]Aerospace Information Research Institute, Chinese Academy of Sciences, Beijing 100190, China
[2]National Key Laboratory of Microwave Imaging Technology, Beijing 100190, China
[3]School of Electronic, Electrical and Communication Engineering, University of Chinese Academy of Sciences, Beijing 100049, China
[4]Qilu Research Institute, Aerospace Information Research Institute, Jinan 250101, China

Corresponding author: Liangjiang Zhou (ljzhou@mail.ie.ac.cn)

This work was supported in part by the National Key Research and Development Program of China under Grant 2017YFC0822400, and in part by the National Natural Science Foundation of China under Grant 61991420, Grant 61991421, and Grant 61991424.

ABSTRACT Airborne SAR tomography (TomoSAR) 3D image reconstruction can be realized with combination of 2D imaging algorithms and compressed sensing (CS) algorithms. However, most typical CS algorithms cannot achieve a balance between algorithm efficiency and 3D reconstruction accuracy. Due to difficulties in flight path control of airborne SAR, it is hard to realize registration of SAR images with frequency-domain imaging algorithms because of time-varying baseline. To address these problems, an efficient 3D image reconstruction method for airborne TomoSAR based on back projection (BP) algorithm and improved adaptive iterative shrinkage-thresholding algorithm (IA-ISTA) is proposed. First, 2D images are achieved with BP algorithm on the ground plane. After registration of SAR images, 3D image reconstruction results in the elevation direction are realized with IA-ISTA. Selection criterion of IA-ISTA parameters are given in this paper. At last, final 3D image reconstruction results are achieved after geometrical transformation based on geometric relationship. Both simulated data and measured data of a P-band airborne TomoSAR system are used. 3D image reconstruction results show that the proposed method outperforms traditional methods regarding efficiency and accuracy, which proves the validity and practicality of the proposed method.

INDEX TERMS Airborne SAR tomography (TomoSAR), 3D image reconstruction, compressed sensing (CS), iterative shrinkage-thresholding algorithm (ISTA), back projection (BP) algorithm.

I. INTRODUCTION

Due to SAR imaging mechanism, there are serious problems of layovers and shadows, which hinder the interpretation, application, and development of SAR remote sensing. With the increasing demand for acquisition of three-dimensional structure information, it is very meaningful to develop 3D imaging techniques, which are significant to 3D environment construction, target interpretation, and biomass estimation [1]–[4]. SAR tomography (TomoSAR) is a classical 3D imaging technique, which forms synthetic aperture in the elevation direction with repeated trajectories. TomoSAR has 3D imaging ability with multiple observations in the elevation direction [5], [6]. The first airborne TomoSAR experiment was conducted by Deutsches Zentrum für Luft- und Raumfahrt (DLR) [7]. After years of development, the Wiener-SVD algorithm was proposed and compared with traditional FFT based 3D image reconstruction methods in TomoSAR. Besides, tomographic results of high resolution TerraSAR-X images were achieved by applying compressed sensing (CS) theory in TomoSAR [8]–[11].

TomoSAR 3D image reconstruction can be mainly divided into two stages. The first stage is high-accuracy 2D imaging and preprocessing, because prerequisite of 3D image reconstruction is the registration of multi-pass SAR images. The second stage is 3D image reconstruction in the elevation direction, in which CS algorithms have been widely applied.

The associate editor coordinating the review of this manuscript and approving it for publication was Brian Ng.

In the first stage of TomoSAR 3D image reconstruction, 2D SAR images are usually obtained with frequency-domain imaging algorithms on the azimuth and range plane. However, in an airborne system, due to atmospheric turbulences, it is very difficult for airborne SAR to control the flight path accurately [12]. With nonideal trajectories and frequency-domain imaging algorithms, realizing image registration of SAR is very difficult. Back projection (BP) algorithm is a time-domain imaging algorithm on the ground plane. Imaging with BP algorithm can remove flat-earth phase and realize image registration automatically, because imaging grids are uniformly defined on the latitude and longitude coordinate system [13]. In this paper, 3D image reconstruction model with BP algorithm will be introduced and the imaging results will be analysed in detail. Based on BP algorithm, construction of the sensing matrix and 3D image reconstruction process are illustrated.

In the second stage of TomoSAR 3D image reconstruction, greedy algorithms and convex optimization algorithms are typical kinds of CS algorithms, which can be applied in TomoSAR 3D image reconstruction in the elevation direction. Orthogonal matching pursuit (OMP) [14] and basis pursuit de-noising (BPDN) [15] are representative algorithms of these two kinds, respectively. However, 3D image reconstruction performance based on OMP are affected by the sparsity K, because iteration number of OMP is mainly determined by sparsity K in theory. On the contrary, BPDN has higher 3D reconstruction accuracy in the elevation direction, but a large number of matrix inversion make it time-consuming. Traditional iterative shrinkage-thresholding algorithm (ISTA) [16] can be realized without prior information about the sparsity K, which does not contain any matrix inversion at the same time.

In order to improve algorithm efficiency of ISTA, a fast iterative shrinkage-thresholding algorithm (FISTA) [17], [18] was proposed, which has been successfully applied in SAR tomography [19]. Besides, element-wise adaptive thresholds for learned ISTA and ISTA with adaptive threshold were analysed in theory [20]. In this paper, we propose an improved adaptive ISTA (IA-ISTA) in 3D image reconstruction of airborne SAR tomography. A specific adaptive threshold and parameter selection criterion of proposed algorithm will be clearly given.

In summary, we present an efficient 3D image reconstruction method for airborne TomoSAR based on BP algorithm and IA-ISTA. Firstly, we will introduce 3D image reconstruction model and give out 3D image reconstruction process based on BP algorithm and compressed sensing algorithm. Secondly, we propose and apply IA-ISTA in 3D image reconstruction of airborne SAR tomography. Compared with traditional methods, proposed IA-ISTA converges much faster without deteriorating 3D image reconstruction performance. Finally, we compare the 3D reconstruction accuracy and algorithm efficiency among results with OMP, traditional ISTA, and proposed IA-ISTA. 3D image reconstruction results of both simulated and measured data of a P-band airborne TomoSAR system are presented to prove effectiveness of our proposed method.

The remainder of this paper is arranged as follows. In Section II, TomoSAR 3D image reconstruction theory based on BP algorithm is introduced and analysed in detail. Then, 3D image reconstruction algorithm for airborne TomoSAR based on IA-ISTA is proposed in Section III. Comparison among 3D image reconstruction results with OMP, traditional ISTA, and proposed IA-ISTA will be detailed shown in section IV with simulated data. In section V, measured data of a P-band airborne TomoSAR system conducted by Aerospace Information Research Institute, Chinese Academy of Sciences (AIRCAS) are adopted and analysis of reconstruction results prove the effectiveness of our proposed method. Finally, conclusions are drawn in Section VI.

II. ANALYSIS OF 3D IMAGE RECONSTRUCTION MODEL WITH BP ALGORITHM

The imaging geometry of SAR tomography with BP algorithm is compendiously shown in Fig. 1, which consists of M linear trajectories with look angle $\alpha_m (m = 1, 2, 3, \ldots, M)$. The average look angle of these different trajectories is $\bar{\alpha}$.

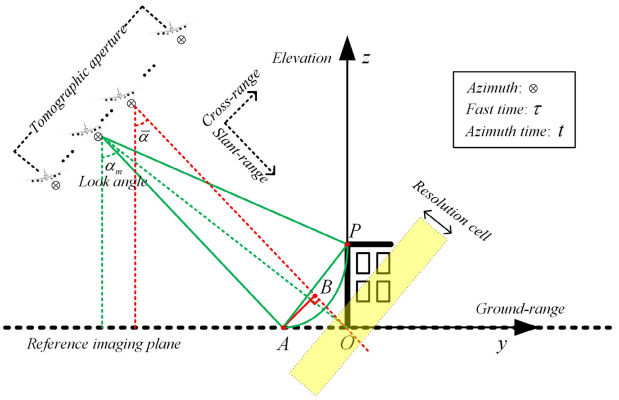

FIGURE 1. Imaging geometry of SAR tomography with BP algorithm.

Radar transmits chirp signal with carrier frequency f_0, pulse width T_p, chirp rate K_r, and signal bandwidth B_w, which is expressed as follows

$$s_t(\tau) = \text{rect}(\frac{\tau}{T_p}) \cdot \exp(j \cdot \pi K_r \tau^2) \tag{1}$$

where rect$(\cdot)$ is a gate function.

Time-domain echo signals of target P in the imaging scene can be expressed as follows

$$s_{r1}(\tau, t) = \sigma_0 \cdot \omega_r(\tau - 2R_p(t)) \cdot \omega_a(t - t_c) \cdot \exp(j \cdot \pi K_r(\tau - \frac{2R_p(t)}{c})^2) \cdot \exp(-j \cdot \frac{4\pi R_p(t)}{\lambda}) \tag{2}$$

where λ represents the wavelength of radar, $\omega_r(\cdot)$ and $\omega_a(\cdot)$ are gate functions, σ_0 is the backscattering coefficient of target P, and $R_p(t)$ is the distance between radar and target P at the azimuth time t.

After range compression, time-domain echo signals can be expressed as below

$$s_{r2}(\tau, t) = \sigma_0 \cdot \omega_a(t - t_c) \cdot \mathrm{sinc}(B_w \cdot (\tau - \frac{2R_p(t)}{c})) \cdot \exp(-j \cdot \frac{4\pi R_p(t)}{\lambda}) \tag{3}$$

2D images are achieved with BP algorithm after the reference imaging plane is uniformly divided into $N_u \times N_v$ imaging grids. Top view of the imaging geometry with BP algorithm is shown in Fig. 2.

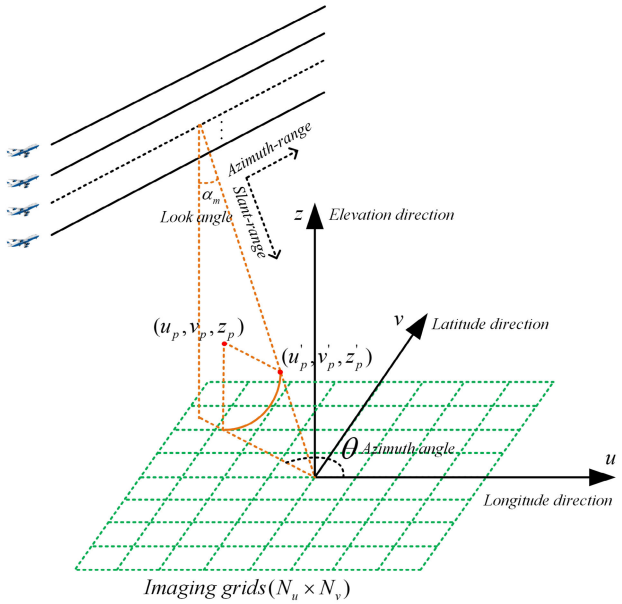

FIGURE 2. Top view of the imaging geometry with BP algorithm.

Flat-earth phase can be regarded as the phase caused by reference imaging plane. After removing the flat-earth phase $\exp(j \cdot 4\pi R_g(t)/\lambda)$ and finishing BP interpolation, the coherent accumulation results of multiple pulses at the imaging grid (u, v, z_{ref}) is shown as below

$$\begin{aligned} Im(u, v) &= \sum_t s_{r2}(\tau, t) \cdot \exp(j \cdot \frac{4\pi R_g(t)}{\lambda}) \\ &= \sum_t \sigma_0(u, v) \cdot \omega_a(t - t_c) \cdot \mathrm{sinc}(B_w(\tau - \frac{2R_p(t)}{c})) \\ &\quad \cdot \exp(-j \cdot \frac{4\pi R_p(t)}{\lambda}) \cdot \exp(j \cdot \frac{4\pi R_g(t)}{\lambda}) \end{aligned} \tag{4}$$

where z_{ref} is the height of reference imaging plane, and $R_g(t)$ is the distance between radar and the imaging grid (u, v, z_{ref}) at the azimuth time t in Fig. 2.

As we can see from Fig. 1, target P is projected onto imaging result A in the 2D image with look angle α_m. In the far field hypothesis, we can assume that $\angle OAP$ is α_m and length l_{OA} can be approximately expressed as below

$$l_{\mathrm{OA}} = z_p \cdot \cot\alpha_m \tag{5}$$

As is shown in Fig. 1, the virtual trajectory with average look angle $\bar{\alpha}$ is represented as the reference trajectory. Imaging result A of different trajectories can be projected onto B in the slant range of the reference trajectory. Therefore, we can achieve different length l_{OB} in TomoSAR trajectories with different incident angles. After registration of 2D images generated from different trajectories, the phase difference $\exp(-j \cdot 4\pi/\lambda \cdot l_{\mathrm{OB}})$ caused by l_{OB} at the same pixel of 2D images can be exploited to estimate the height z_p in the elevation direction [21]–[23].

$$l_{\mathrm{OB}} = l_{\mathrm{OA}} \cdot \sin\bar{\alpha} = z_p \cdot \cot\alpha_m \cdot \sin\bar{\alpha} \tag{6}$$

According to the above analysis, the final 2D BP imaging results at the imaging grid (u, v, z_{ref}) of different trajectories can be approximately expressed as below

$$Im(u, v) = \sum_p \sigma_0(u, v) \cdot \exp(-j \cdot \frac{4\pi}{\lambda} \cdot z_p \cdot \sin\bar{\alpha} \cdot \cot\alpha_m) \tag{7}$$

Because 2D images are achieved with BP algorithm on the ground plane, there are geometric distortions in the 3D image reconstruction results. As is shown in Fig. 2, (u_p, v_p, z_p) is the direct 3D reconstruction result. Compared with accurate spatial location (u_p', v_p', z_p'), height z_p is accurate, but the horizontal coordinates (u_p, v_p) are wrong. Therefore, geometrical transformation should be finished after 3D image reconstruction with compressed sensing algorithms. After these manipulations, (u_p', v_p', z_p') can be calculated as below

$$u_p' = u_p - z_p \cdot \cot\bar{\alpha} \cdot \sin\theta \tag{8}$$

$$v_p' = v_p - z_p \cdot \cot\bar{\alpha} \cdot \cos\theta \tag{9}$$

$$z_p' = z_p \tag{10}$$

In summary, processing chain of TomoSAR 3D image reconstruction based on BP algorithm and proposed IA-ISTA is evocatively illustrated in Fig. 3 and Fig. 4. Flowchart of TomoSAR 3D image reconstruction process mainly consists of the following 4 steps.

step1: We receive raw echo signals of the targets to be reconstructed in different trajectories of airborne TomoSAR.

step2: 2D BP images are achieved after range compression of echo signals, flat-earth phase removing, and BP interpolation by using (3) and (4).

step3: We finish registration of 2D BP images for preparation of 3D image reconstruction [24], [25]. Then, 3D image reconstruction of airborne TomoSAR is realized with proposed IA-ISTA, in which the sensing matrix is obtained from (7).

step4: Final 3D image reconstruction results are achieved after geometrical transformation according to the geometric relationship.

III. IA-ISTA BASED 3D IMAGE RECONSTRUCTION

A. TRADITIONAL ISTA

For 3D image reconstruction of SAR tomography with BP algorithm, the compressed sensing can be expressed as below

$$\boldsymbol{y} = \Phi \cdot \boldsymbol{x} + \boldsymbol{\varepsilon} \tag{11}$$

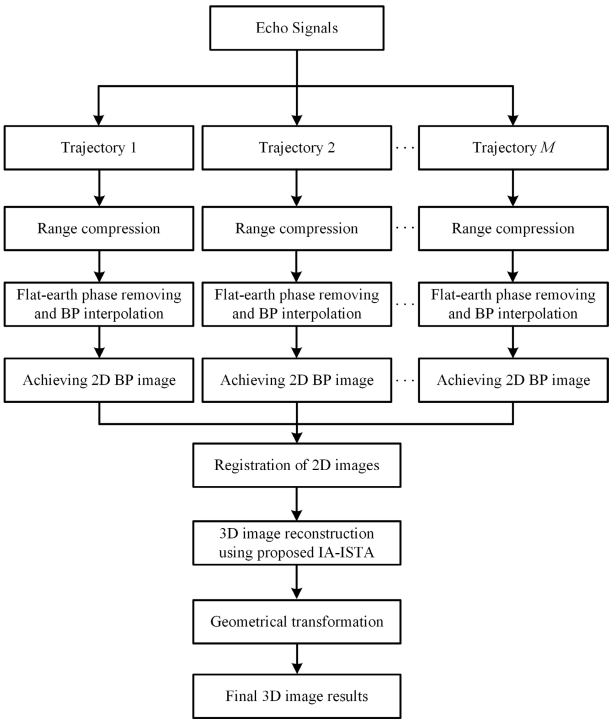

FIGURE 3. Flowchart of 3D image reconstruction process of SAR tomography with BP algorithm and proposed IA-ISTA on the ground plane.

where $\boldsymbol{y}$ is a measurement vector of the same pixel $Im(u, v)$ in the registered 2D image stack, $\boldsymbol{x}$ is a vector to be reconstructed in the elevation direction, and $\boldsymbol{\varepsilon}$ is the noise vector. According to (7), Φ is an $M \times N_z$ sensing matrix with

$$\phi_{mn} = \exp(-j \cdot \frac{4\pi}{\lambda} \cdot z_n \cdot \sin\bar{\alpha} \cdot \cot\alpha_m) \tag{12}$$

in which $z_n (n = 1, 2, 3, \ldots, N_z)$ is the sampling grids in the elevation direction.

Considering the Lasso problem [15], [26], equation (11) can be described as the following problem

$$\min_{\boldsymbol{x}} \quad \frac{1}{2} \|\boldsymbol{y} - \Phi \cdot \boldsymbol{x}\|_2^2 + \zeta \|\boldsymbol{x}\|_1 \tag{13}$$

where ζ is the Lagrange multiplier.

In traditional ISTA, $\boldsymbol{x}^{k+1}$ is calculated as below after initializing parameters

$$\boldsymbol{x}_{\text{new}}^k = \boldsymbol{x}^k - \frac{1}{L} \cdot \Phi^{\text{H}}(\Phi \cdot \boldsymbol{x}^k - \boldsymbol{y}) \tag{14}$$

$$\boldsymbol{x}^{k+1} = \eta(\boldsymbol{x}_{\text{new}}^k) = \text{sign}(\boldsymbol{x}_{\textbf{new}}^k) \cdot \max(|\boldsymbol{x}_{\textbf{new}}^k| - \mu, 0) \tag{15}$$

where $\eta(\cdot)$ is the shrinkage function, $\text{sign}(\boldsymbol{x})$ is the symbolic function, μ is the threshold used for traditional ISTA, Φ^{H} represents the conjugate transpose operation of Φ, and L is a constant that should be larger than the max eigenvalue of $\Phi^{\text{H}}\Phi$.

B. IMPROVED ADAPTIVE ISTA

Compared with traditional ISTA, proposed IA-ISTA can be applied as a superior 3D image reconstruction algorithm for airborne SAR tomography because of both having accurate reconstruction results and better algorithm efficiency.

The novel modification of proposed IA-ISTA is that an adaptive threshold $T(\boldsymbol{x}, \mu, a)$ is adopted to calculate $\boldsymbol{x}^{k+1}$ in (15) instead of a constant μ in traditional ISTA.

Firstly, IA-ISTA doesn't need the sparsity K as a prior information for TomoSAR 3D image reconstruction. Secondly, IA-ISTA uses $T(\boldsymbol{x}, \mu, a)$ as an adaptive threshold in the shrinkage function $\eta(\cdot)$ instead of the constant μ in traditional ISTA, which can greatly increase the rate of convergence.

In proposed IA-ISTA, $\boldsymbol{x}^{k+1}$ is calculated as below after initializing parameters

$$\boldsymbol{x}_{\text{new}}^k = \boldsymbol{x}^k - \frac{1}{L} \cdot \Phi^{\text{H}}(\Phi \cdot \boldsymbol{x}^k - \boldsymbol{y}) \tag{16}$$

$$\boldsymbol{x}^{k+1} = \eta(\boldsymbol{x}_{\text{new}}^k) = \text{sign}(\boldsymbol{x}_{\textbf{new}}^k) \cdot \max(|\boldsymbol{x}_{\textbf{new}}^k| - T(\boldsymbol{x}_{\textbf{new}}^k, \mu, a), 0) \tag{17}$$

In IA-ISTA, $\boldsymbol{x}$ gets refreshed along with the iteration of algorithm. When the algorithm converges, $\boldsymbol{x}^{k+1} \approx \boldsymbol{x}^k$ and $\boldsymbol{x}_{\textbf{new}}^k \approx \boldsymbol{x}^k$. According to (16) and (17), $\boldsymbol{x}^k$ should satisfy the following condition

$$\boldsymbol{x}^k \approx \text{sign}(\boldsymbol{x}^k) \cdot \max(|\boldsymbol{x}^k| - T(\boldsymbol{x}^k, \mu, a), 0) \tag{18}$$

If $T(\boldsymbol{x}, \mu, a)$ is a function which converges to 0 when $\boldsymbol{x}$ gradually becomes larger as the algorithm iterates, the algorithm will converge more quickly [20]. In this paper, we propose an adaptive threshold which is defined below

$$T(\boldsymbol{x}, \mu, a) = \mu/(|\boldsymbol{x}|/a + 1) \tag{19}$$

The gradient of adaptive threshold $T(\boldsymbol{x}, \mu, a)$ with respect to $\boldsymbol{x}$ is calculated as below

$$\nabla T(\boldsymbol{x}, \mu, a)/\nabla \boldsymbol{x} = -\mu \cdot \text{sign}(\boldsymbol{x})/(|\boldsymbol{x}|/\sqrt{a} + \sqrt{a})^2 \tag{20}$$

In gradient (20), both parameter μ and a determine the sparsity of IA-ISTA, and rate of convergence in IA-ISTA is mainly determined by parameter a. Parameter selection in IA-ISTA is illustrated as follows.

1) L is a constant which should be larger than the max eigenvalue of $\Phi^{\text{H}}\Phi$.
2) Predefined tolerance δ is a very small non-negative number which determines the number of iterations.
3) In the proposed adaptive threshold $T(\boldsymbol{x}, \mu, a)$, parameter μ and a are small non-negative numbers. In this paper, μ is set to $0.01 \times |y_{\text{ref}}|$, and a is set to $0.1 \times |y_{\text{ref}}|$, where y_{ref} is an element chosen from the measurement vector $\boldsymbol{y}$.

The whole processing chain of 3D image reconstruction algorithm for airborne TomoSAR based on IA-ISTA is shown in Table 1.

Firstly, we input the measurement vector $\boldsymbol{y}$, the sensing matrix Φ with $\phi_{mn} = \exp(-j \cdot 4\pi/\lambda \cdot z_n \cdot \sin\bar{\alpha} \cdot \cot\alpha_m)$, and number of iterations N_i.

Secondly, initialization of all the parameters in IA-ISTA is finished.

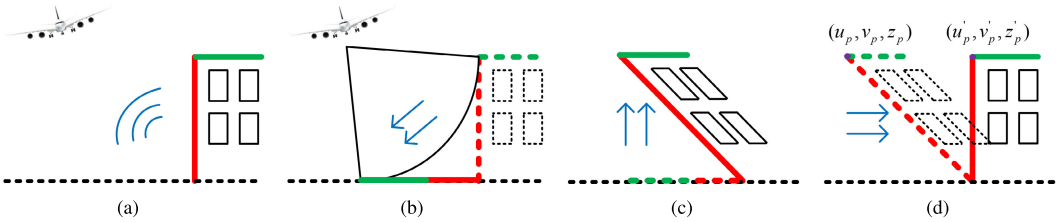

FIGURE 4. Diagram of 3D image reconstruction process of SAR tomography with BP algorithm and proposed IA-ISTA on the ground plane: (a) echo signals of 3D targets to be reconstructed, (b) 2D imaging process with BP algorithm on the ground plane, (c) 3D image reconstruction results using proposed IA-ISTA, (d) final 3D image reconstruction results after geometrical transformation.

TABLE 1. IA-ISTA based 3D image reconstruction algorithm.

Input: $\boldsymbol{y}$, Φ with $\phi_{mn} = \exp(-j \cdot 4\pi/\lambda \cdot z_n \cdot \sin\bar{\alpha} \cdot \cot\alpha_m)$, and number of iterations N_i

Initialization: L, δ, $k = 0$, $T(\boldsymbol{x}, \mu, a) = \mu/(|\boldsymbol{x}|/a + 1)$, and $\boldsymbol{x}^0 = 0$

Iteration:

(1) $\boldsymbol{x}^k_{\text{new}} = \boldsymbol{x}^k - \frac{1}{L} \cdot \Phi^{\text{H}}(\Phi \cdot \boldsymbol{x}^k - \boldsymbol{y})$
(2) $\boldsymbol{x}^{k+1} = \text{sign}(\boldsymbol{x}^k_{\textbf{new}}) \cdot \max(|\boldsymbol{x}^k_{\textbf{new}}| - T(\boldsymbol{x}^k_{\textbf{new}}, \mu, a), 0)$
(3) if $\left\|\boldsymbol{x}^{k+1} - \boldsymbol{x}^k\right\|_2 < \delta$ or $k + 1 = N_i$
stop iteration
else
$k = k + 1$, go to iteration (1)

Output: 3D image reconstruction result $\boldsymbol{x}^{k+1}$

Thirdly, (16) and (17) are adopted in the iteration of IA-ISTA, in which the shrinkage function $\eta(\cdot)$ gets adaptively refreshed while $\boldsymbol{x}^k$ is refreshing. When the number of iterations is larger than the threshold or the relative error $\left\|\boldsymbol{x}^{k+1} - \boldsymbol{x}^k\right\|_2$ is smaller than the predefined tolerance δ, 3D image reconstruction process based on IA-ISTA should be automatically terminated.

Finally, $\boldsymbol{x}^k$ is the reconstruction result of SAR tomography in the elevation direction.

TABLE 2. Simulation parameters.

Parameters	Values
Carrier frequency f_0 (GHz)	1.5
Bandwidth B_w (MHz)	200
Pulse width T_p (μs)	10
Chirp rate K_r (Hz/s)	2×10^{13}
Azimuth angle θ (°)	0
Slant range of the middle trajectory R (m)	3000
Synthetic aperture L_s (m)	300
Average look angle $\bar{\alpha}$ (°)	45
Look angles of different trajectories α_m (°)	45.683, 45.545, 45.408, 45.271, 45.135, 45.000, 44.865, 44.731, 44.598, 44.465, 44.333

IV. SIMULATED RESULTS

A. SIMULATION CONFIGURATION

The simulation parameters are enumerated in Table 2. Considering unambiguous height in the elevation direction of airborne TomoSAR [23], we choose chirp signals at L-band for simulation with carrier frequency $f_0 = 1.5$GHz. Simulated observation geometry consists of 11 linear trajectories with average look angle $\bar{\alpha} = 45°$. Slant range of the middle trajectory is set to 3000m and the height interval of the 11 trajectories in the elevation direction is set to 10m, so the calculation results of look angles of different trajectories are shown in Table 2. The azimuth angle θ of the TomoSAR equivalent phase center in Fig. 2 is set to 0°. Under the assumption that the length of antenna D is 2m, the synthetic aperture is 300m, which is calculated with

$$L_s = \frac{\lambda \cdot R}{D} \tag{21}$$

B. 3D IMAGE RECONSTRUCTION BASED ON IA-ISTA

Firstly, we achieve 2D SAR images from echo signals of different trajectories by using BP algorithm illustrated in Section II.

Secondly, after registration of 2D SAR images, we then construct sensing matrix Φ according to simulation parameters enumerated in Table 2, which is an $M \times N_z$ sensing matrix with

$$\phi_{mn} = \exp(-j \cdot \frac{4\pi}{\lambda} \cdot z_n \cdot \sin\bar{\alpha} \cdot \cot\alpha_m) \tag{22}$$

TomoSAR 3D image reconstruction can be regarded as the following problem

$$\min_{\boldsymbol{x}} \quad \frac{1}{2} \|\boldsymbol{y} - \Phi \cdot \boldsymbol{x}\|_2^2 + \zeta \|\boldsymbol{x}\|_1 \tag{23}$$

According to the sensing matrix Φ and selection criterion of parameters illustrated in Section III, we can confirm the parameters in proposed IA-ISTA.

With processing chain of proposed IA-ISTA illustrated in Table 1, TomoSAR 3D image reconstruction problem can be solved with the following modificated iterations

$$\boldsymbol{x}^k_{\text{new}} = \boldsymbol{x}^k - \frac{1}{L} \cdot \Phi^{\text{H}}(\Phi \cdot \boldsymbol{x}^k - \boldsymbol{y}) \tag{24}$$

$$\begin{aligned} \boldsymbol{x}^{k+1} &= \eta(\boldsymbol{x}^k_{\text{new}}) \\ &= \text{sign}(\boldsymbol{x}^k_{\textbf{new}}) \cdot \max(|\boldsymbol{x}^k_{\textbf{new}}| - T(\boldsymbol{x}^k_{\textbf{new}}, \mu, a), 0) \end{aligned} \tag{25}$$

where $T(\boldsymbol{x}, \mu, a) = \mu/(|\boldsymbol{x}|/a + 1)$.

$T(\boldsymbol{x}, \mu, a)$ is a proposed specific adaptive threshold in the shrinkage function $\eta(\cdot)$ instead of the constant μ in traditional

ISTA, which gets automatically refreshed in the iterations (24) and (25) along with the change of $\boldsymbol{x}$.

After 3D image reconstruction with proposed IA-ISTA, final TomoSAR 3D image reconstruction results can be achieved with geometrical transformation by using (8), (9), and (10).

C. ANALYSIS OF RESOLUTION

Theoretical resolutions of 2D images and 3D image reconstruction results can be calculated as below

$$\rho_a = \frac{D}{2} \tag{26}$$

$$\rho_r = \frac{c}{2 \cdot B_w \cdot \sin\bar{\alpha}} \tag{27}$$

$$\rho_z = \frac{\lambda \cdot R}{2 \cdot L_z \cdot \sin\bar{\alpha}} \tag{28}$$

where L_z is the tomographic aperture, ρ_a is the resolution in the azimuth range, ρ_r is the resolution in the ground range, and ρ_z is the resolution in the elevation direction. Using simulation parameters in Table 2, ρ_a is calculated as 1m, ρ_r is calculated as 1.06m, and ρ_z is calculated as 3m.

Proposed IA-ISTA is a modification of traditional ISTA, which can achieve super resolution in the elevation direction. However, it is very complicated to find the super resolution of proposed IA-ISTA. Therefore, we conduct Monte Carlo simulation to detect two scatterers with different distance in the elevation direction. The definition of a successful detection is refered to [11]. When the detection rate of Monte Carlo simulation is 0.5, we can consider the distance between the two scatterers as the super resolution of proposed IA-ISTA. Figure 5 is the detection rate along with the change of distance between the two scatterers with different SNR. In Fig. 5, the detection rate is affected by the change of SNR. When the detection rate is 0.5, super resolution of proposed IA-ISTA in the elevation direction is around 0.5m.

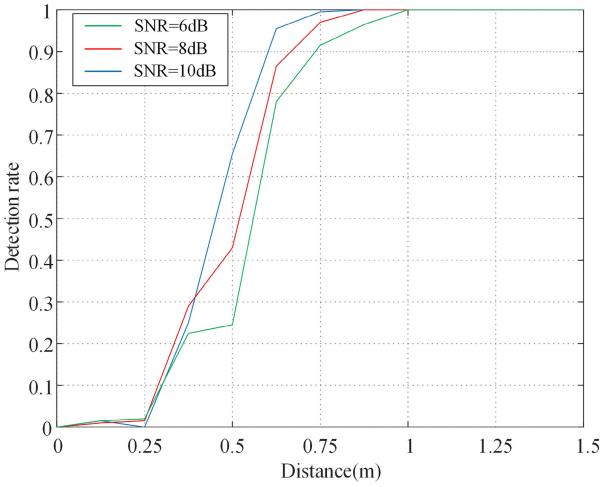

FIGURE 5. Detection rate along with the change of distance between the two scatterers with different SNR.

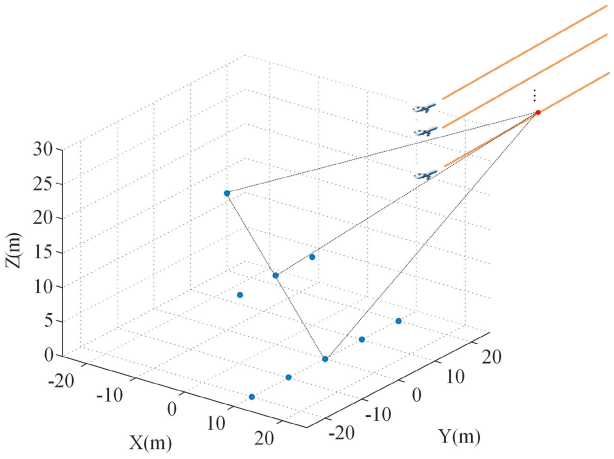

FIGURE 6. Simulated point scatterers located in the geodetic coordinate system.

D. RESULTS OF SIMULATED POINT SCATTERERS

The simulated point scatterers are shown in Fig. 6, which are located in the geodetic coordinate system. The imaging scene on the ground plane is set up as 50m × 50m, which is uniformly separated into 501 × 501 grids with an interval being 0.1m × 0.1m. In this simulation, we add Gaussian white noise with SNR being −10dB.

Figure 7 is the 2D image of simulated point scatterers using BP algorithm with SNR being −10dB. As we can see from Fig. 7, simulated point scatterers with height 0m, 10m, and 20m in Fig. 6 are projected onto point A framed in Fig. 7 due to layovers.

In the simulated results, L in (11) is set to 250. Sampled elevation position z_n in (12) ranges from −2m to 23m with an interval being 0.125m.

OMP, traditional ISTA and proposed IA-ISTA are adopted for 3D image reconstruction of the pixel (10m,0m) in point A. When the algorithms converge, number of iterations is represented as N_i. Iteration number of traditional ISTA is much bigger than that of proposed IA-ISTA, so we use $lg(N_i)$ to represent N_i. Figure 8 is the needed number of iterations using traditional ISTA and proposed IA-ISTA when the algorithms converge along with the change of predefined tolerance δ, which shows that proposed IA-ISTA has much better rate of convergence with the same predefined tolerance δ than traditional ISTA and greatly improves algorithm efficiency.

In 3D image reconstruction process with OMP, sparsity K is set to 2 and 3, respectively. In 3D image reconstruction process with traditional ISTA and proposed IA-ISTA, L in (14) and (16) is set to 250 and the predefined tolerance δ is set to 10^{-3}.

3D image reconstruction results of the pixel (10m,0m) in point A with different algorithms are shown in Fig. 9. In Fig. 9, simulated point scatterers can be accurately distinguished at their actual height 0m, 10m, and 20m. We use mean squared error (MSE), mean absolute error (MAE), and structural similarity (SSIM) to evaluate the accuracy of

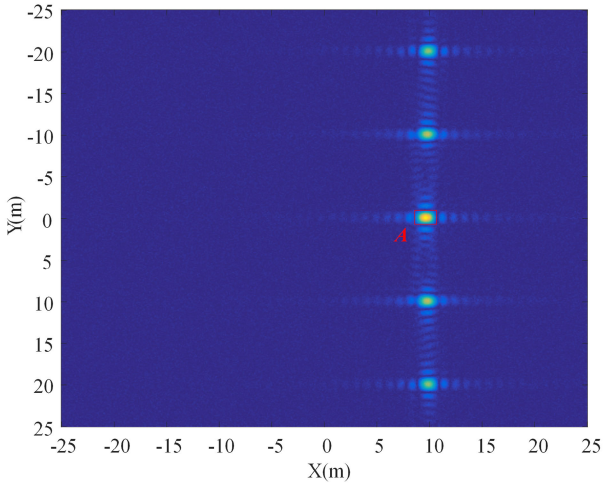

FIGURE 7. 2D image of simulated point scatterers using BP algorithm with SNR being −10dB (*A* is the layover position of 3 scatterers with different heights).

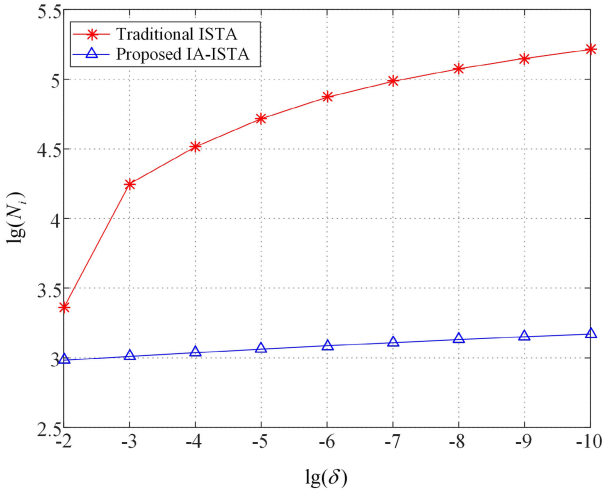

FIGURE 8. Needed number of iterations N_i along with the change of predefined tolerance δ.

TABLE 3. Evaluation of 3D image reconstruction results.

Algorithm	OMP(K=2)	OMP(K=3)	ISTA	IA-ISTA
MSE	0.0242	0.0286	0.0182	0.0194
MAE	0.0245	0.0292	0.0204	0.0199
SSIM	0.9473	0.9429	0.9454	0.9440

reconstruction results [27], which is shown in Table 3. From Fig. 9 and Table 3, we can see that 3D image reconstruction results with IA-ISTA and traditional ISTA are similar, which are better than 3D image reconstruction results with OMP. SSIM of 3D image reconstruction results with these algorithms are similar, but MSE and MAE of 3D image reconstruction results with traditional ISTA and proposed IA-ISTA are both better than the 3D image reconstruction results with OMP.

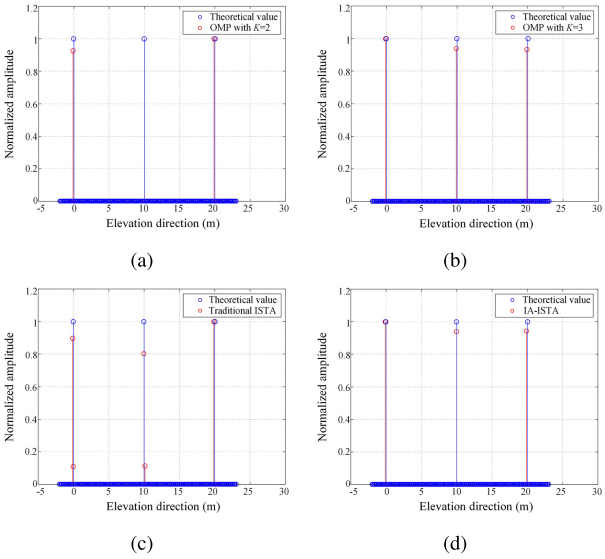

FIGURE 9. 3D image reconstruction results: (a) OMP with sparsity $K = 1$, (b) OMP with sparsity $K = 2$, (c) traditional ISTA, (d) proposed IA-ISTA.

With proposed IA-ISTA, 3D image reconstruction results of the simulated point scatterers are shown in Fig. 10. Figure 10(a) is the direct 3D image reconstruction results with proposed IA-ISTA. And, Fig. 10(b) is the 3D image reconstruction results after geometrical transformation by using (8), (9), and (10). In Fig. 10, we can see that 3D image reconstruction results of simulated point scatterers will be located at their actual positions after geometrical transformation.

E. RESULTS OF SIMULATED BUILDING

The simulated building is shown in Fig. 11, which is located in the geodetic coordinate system. Colorbar of Fig. 11 represents height of the simulated building. The imaging scene on the ground plane is set up as 50m × 50m, which is uniformly separated into 501 × 501 grids with an interval being 0.1m × 0.1m.

In the simulated results, sampled elevation position z_n in (12) ranges from −2m to 23m with an interval being 0.125m. OMP, traditional ISTA, and proposed IA-ISTA are adopted for 3D image reconstruction of the simulated building. In 3D image reconstruction process by using OMP, sparsity K is set to 3. In 3D image reconstruction process with elevation resolution $\rho_z = 3m$ by using traditional ISTA and proposed IA-ISTA, L in (14) and (16) is set to 250 and the predefined tolerance δ is set to 10^{-3}. In 3D image reconstruction process with elevation resolution $\rho_z = 6m$ by using traditional ISTA and proposed IA-ISTA, L in (14) and (16) is set to 500 and the predefined tolerance δ is set to 10^{-3}.

Figure 12 is the 3D image reconstruction results with different elevation resolution ρ_z by using OMP, traditional ISTA, and proposed IA-ISTA after geometrical transformation,

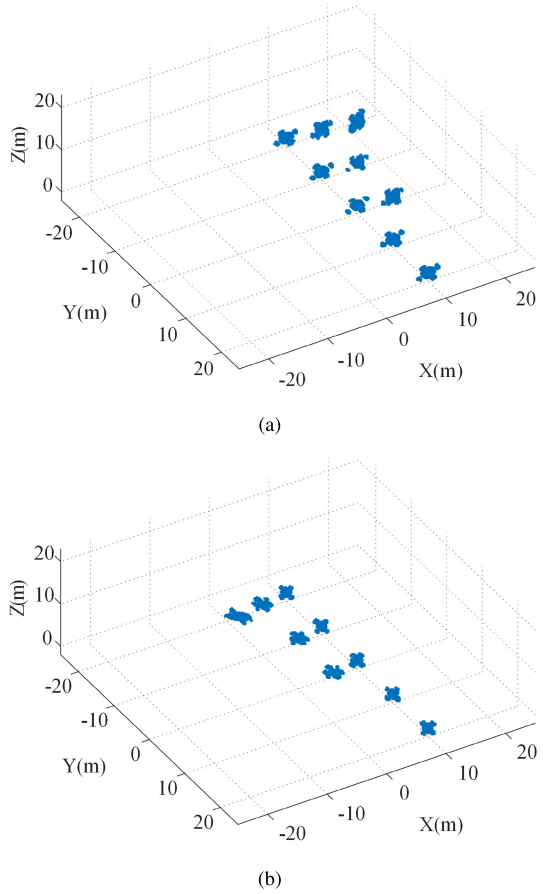

FIGURE 10. 3D image reconstruction results of simulated point scatterers with proposed IA-ISTA: (a) before geometrical transformation, (b) after geometrical transformation.

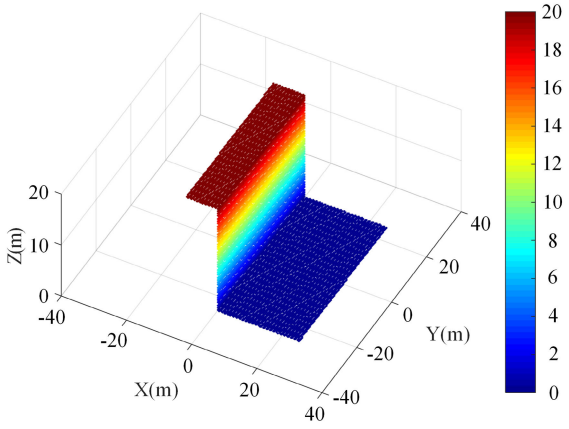

FIGURE 11. Simulated building located in the geodetic coordinate system.

in which colorbar represents height of the reconstruction results.

Processing with MATLAB 2016 and CPU intel Xeon 6148, time cost of 3D image reconstruction with traditional ISTA and proposed IA-ISTA is illustrated in Table 4 and Table 5. Under the same simulation configuration, time cost of proposed IA-ISTA is much smaller than that of traditional ISTA.

TABLE 4. Time cost of traditional ISTA and proposed IA-ISTA ($\rho_z = 3m$).

Algorithm	traditional ISTA	proposed IA-ISTA
Time cost (s)	4401.394	1520.340

TABLE 5. Time cost of traditional ISTA and proposed IA-ISTA ($\rho_z = 6m$).

Algorithm	traditional ISTA	proposed IA-ISTA
Time cost (s)	2014.738	1312.947

TABLE 6. Evaluation of 3D image reconstruction results ($\rho_z = 3m$).

Algorithm	OMP($K = 3$)	traditional ISTA	proposed IA-ISTA
MSE	0.0067	0.0061	0.0058
MAE	0.0071	0.0065	0.0060
SSIM	0.9663	0.9649	0.9653
3D entropy	0.2972	0.2052	0.2084

TABLE 7. Evaluation of 3D image reconstruction results ($\rho_z = 6m$).

Algorithm	OMP($K = 3$)	traditional ISTA	proposed IA-ISTA
MSE	0.0078	0.0069	0.0068
MAE	0.0083	0.0071	0.0068
SSIM	0.9569	0.9532	0.9580
3D entropy	0.3149	0.2338	0.2362

We use MSE, MAE, SSIM, and 3D entropy to evaluate 3D image reconstruction results with different algorithms, which is shown in Table 6 and Table 7. 3D entropy of reconstruction results is defined as below

$$P(i,j) = \frac{\chi(i,j)}{(N_u \times N_v \times N_z)} \tag{29}$$

$$H = -\sum_{i=0}^{255}\sum_{j=0}^{255} P(i,j) \cdot ln(P(i,j)) \tag{30}$$

where (i,j) is combination of the pixel grey level value $i(0 \leq i \leq 255)$ and the local mean of neighbour domain $j(0 \leq j \leq 255)$ which the pixel belongs to. $\chi(i,j)$ is the statistical quantity of (i,j). In this paper, we calculate j by using the local $3 \times 3 \times 3$ pixels.

Consistent with results of simulated point scatterers, SSIM of 3D image reconstruction results with these algorithms are similar, but MSE, MAE, and 3D entropy of 3D image reconstruction results with traditional ISTA and proposed IA-ISTA are all better than those of the 3D image reconstruction results with OMP. Through the comparison of Table 6 and Table 7, we can find that 3D image reconstruction performance can be affected by the resolution ρ_z in the elevation direction. MSE, MAE, SSIM, and 3D entropy of 3D image reconstruction results with $\rho_z = 3m$ are all better than those of 3D image reconstruction results with $\rho_z = 6m$.

In summary, based on 3D image reconstruction results and analysis of simulated point scatterers and building, we can conclude that proposed IA-ISTA is an effective 3D image reconstruction algorithm in the elevation direction for TomoSAR, which has better rate of convergence and higher

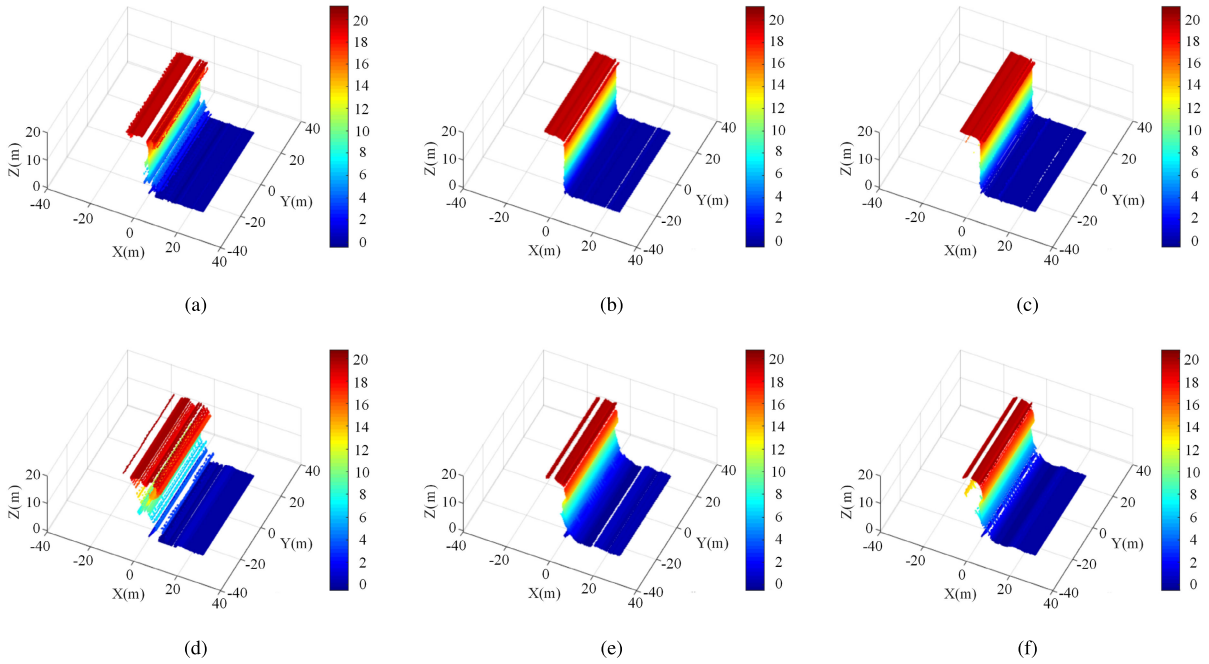

FIGURE 12. 3D image reconstruction results of simulated building after geometrical transformation: (a) OMP with sparsity $K = 3$ ($\rho_z = 3m$), (b) traditional ISTA ($\rho_z = 3m$), (c) proposed IA-ISTA ($\rho_z = 3m$), (d) OMP with sparsity $K = 3$ ($\rho_z = 6m$), (e) traditional ISTA ($\rho_z = 6m$), (f) proposed IA-ISTA ($\rho_z = 6m$).

algorithm efficiency than traditional ISTA under the same experimental conditions and algorithm parameters.

V. EXPERIMENTAL RESULTS

A. EXPERIMENT DESCRIPTION

The airborne SAR tomography experiment at P-band was conducted by AIRCAS in Dunhuang, Gansu province, China, in 2020. The airborne TomoSAR experiment consists of 7 linear trajectories with different look angles, which are as parallel as possible. Optical and SAR images of the imaging area are clearly shown in Fig. 13, in which the imaging targets are buildings with 11 floors and a roof. Height of each floor is around 4m, so height of the building is approximately 50 meters. TomoSAR experiment and system configuration is briefly enumerated in Table 8.

TABLE 8. TomoSAR experiment and system configuration.

Parameters	Values
Carrier frequency f_0 (GHz)	0.39
Bandwidth B_w (MHz)	200
Pulse width T_p (μs)	15
Chirp rate K_r (Hz/s)	1.33×10^{13}
Azimuth angle θ (°)	90
Average look angle $\bar{\alpha}$ (°)	43.566
Look angles of different trajectories α_m (°)	43.217, 43.225, 43.516, 43.520, 43.690, 43.886, 43.910

B. TOMOSAR 3D IMAGE RECONSTRUCTION RESULTS

As is shown in Fig. 13(b), 2D images of the imaging area in different trajectories are achieved with BP algorithm on the ground plane at the reference imaging height 1076m, which is measured by differential GPS.

Before realizing 3D image reconstruction in the elevation direction, a DFT based registration algorithm [24], [25] is applied to finish registration among 2D SAR images of different trajectories, which can realize image registration at sub-pixel level in theory. After normalization, center of the imaging area represents (0m,0m). Figure 14 is the coherence of the imaging area between two trajectories with look angle 43.516° and 43.520° before and after image registration. And, Figure 15 is the statistical histogram of coherence coefficient, which measures complex correlation coefficient between images f and g over an N-pixel local area. The correlation coefficient is defined as follows

$$\gamma = \frac{|\sum_{i=1}^{N} f_i \cdot g_i^{\mathrm{H}}|}{\sqrt{\sum_{i=1}^{N} |f_i|^2 \cdot \sum_{i=1}^{N} |g_i|^2}} \tag{31}$$

As is shown in Fig. 14 and Fig. 15, peak of the coherence coefficient in Fig. 15 increases from 0.73 to 0.98 when N is set to 3×3. The coherence of the imaging area can be greatly improved after registration.

In the experimental results, sampled elevation position z_n in (12) ranges from 1026m to 1226m with an interval being 1m. OMP, traditional ISTA and proposed IA-ISTA are adopted for 3D image reconstruction of the imaging area framed in Fig. 13.

In 3D image reconstruction process with OMP, sparsity K is set to 2. In 3D image reconstruction process with traditional

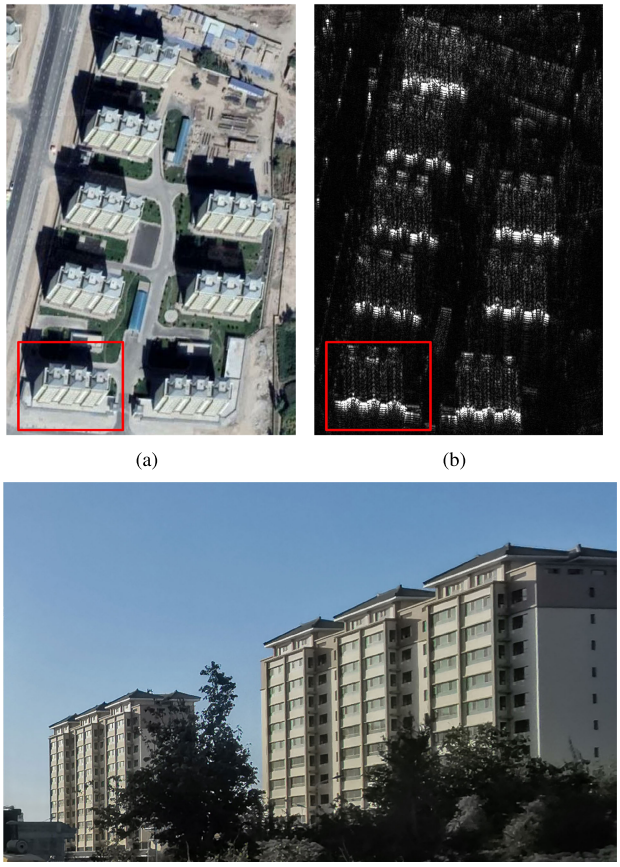

FIGURE 13. Optical and SAR images of the imaging area: (a) optical image visualized in Google-Earth, (b) SAR image with BP algorithm, (c) optical photo taken on the ground.

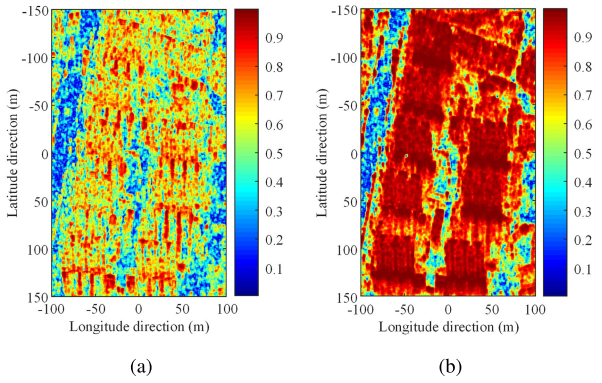

FIGURE 14. Coherence of the imaging area: (a) before registration, (b) after registration.

ISTA and proposed IA-ISTA, L in (14) and (16) is set to 450 and the predefined tolerance δ is set to 0.1.

Figure 16 is the front view and side view of 3D image reconstruction results of the imaging area framed in Fig. 13(b) with different algorithms, in which display threshold of point cloud is 0.03 after normalization and colorbar represents altitude of the imaging area. Processing with MATLAB 2016 and CPU intel Xeon 6148, time cost of 3D image reconstruction

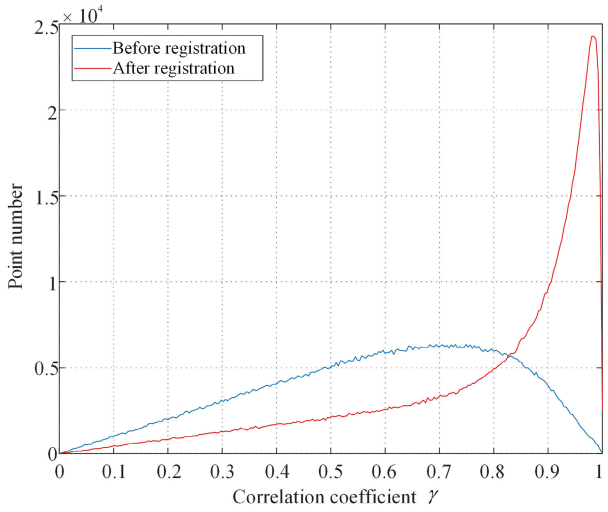

FIGURE 15. Statistical histogram of correlation coefficient.

TABLE 9. Time cost of traditional ISTA and proposed IA-ISTA.

Algorithm	traditional ISTA	proposed IA-ISTA
Time cost (s)	2839.007	337.855

TABLE 10. Evaluation of 3D image reconstruction results.

Algorithm	OMP($K=2$)	traditional ISTA	proposed IA-ISTA
3D entropy	0.8832	0.7076	0.6661

with traditional ISTA and proposed IA-ISTA is illustrated in Table 9.

With proposed IA-ISTA, the final 3D image reconstruction results of the imaging area after geometrical transformation are shown in Fig. 17, in which colorbar represents altitude of the imaging area.

We use 3D entropy to evaluate 3D image reconstruction results with different algorithms, which is shown in Table 10.

Consistent with the simulated results, we can achieve similar and accurate 3D image reconstruction results with traditional ISTA and proposed IA-ISTA, which are both better than that with OMP. Compared with reconstruction results with OMP, 3D entropy of reconstruction results with traditional ISTA and proposed IA-ISTA get effectively decreased. Especially in the side view of 3D image reconstruction results, we can see that there are a lot of outliers at the bottom of reconstructed results with OMP, because the sparsity K of OMP is empirically set to 2, which determines the iteration number of OMP and severely affects the final 3D image reconstruction results. Under the same experimental conditions and algorithm parameters, time cost of traditional ISTA is approximately 8.4 times as large as that of proposed IA-ISTA. In Fig. 17, the imaging area has been well reconstructed with proposed algorithm after geometrical transformation. Height of the reconstruction results is very close to 50m, which is consistent with the real height of buildings with 11 floors and a roof.

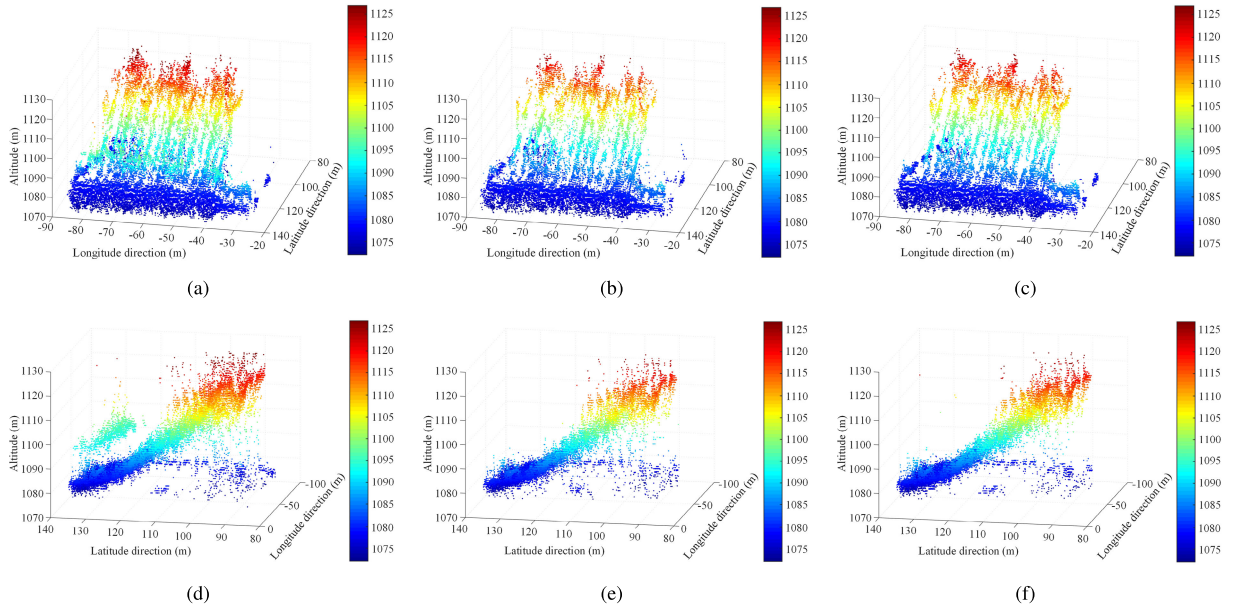

FIGURE 16. Front view and side view of 3D image reconstruction results: (a) front view (OMP with sparsity $K = 2$), (b) front view (traditional ISTA), (c) front view (proposed IA-ISTA), (d) side view (OMP with sparsity $K = 2$), (e) side view (traditional ISTA), (f) side view (proposed IA-ISTA).

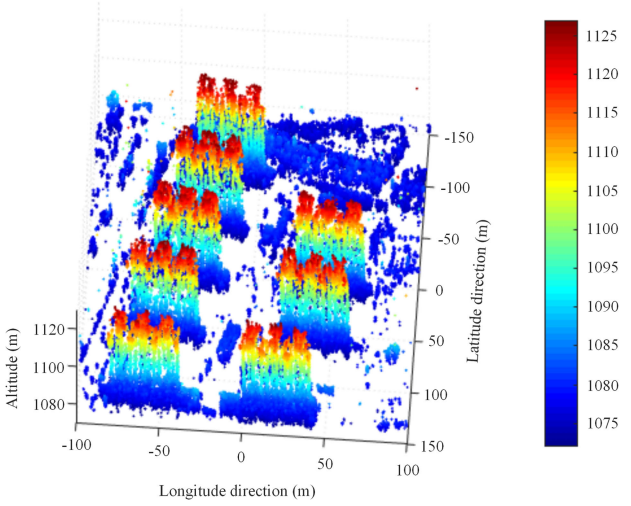

FIGURE 17. Final 3D image reconstruction results of the imaging area with proposed algorithm after geometrical transformation.

In summary, analysis and 3D image reconstruction results of measured data of a P-band TomoSAR system indicate that we can simultaneously improve algorithm efficiency and achieve relatively acurate 3D image reconstruction results by using proposed IA-ISTA.

VI. CONCLUSION

This study set out to find an efficient 3D image reconstruction method for airborne TomoSAR. A novel 3D image reconstruction method adopting back projection algorithm and improved adaptive iterative shrinkage-thresholding algorithm (IA-ISTA) is proposed in this paper, which can take both 3D reconstruction accuracy and speed into account.

First, we introduced TomoSAR 3D image reconstruction model with BP algorithm in details. Based on IA-ISTA and BP algorithm, a novel 3D image reconstruction procedure for airborne TomoSAR is developed, which has better reconstruction performance and algorithm efficiency than traditional methods. At last, analysis and 3D image reconstruction results of both simulated and measured data of a P-band airborne TomoSAR system conducted by AIRCAS validate reconstruction performance and high efficiency of the proposed method.

In our future study, this proposed method will be furtherly applied in 3D image reconstruction of Airborne TomoSAR with multi-azimuth observation angles due to high reconstruction speed and favourable reconstruction results, because panoramic 3D image reconstruction with multi-zimuth observations requires high reconstruction accuracy and contains a tremendous amount of computation.

REFERENCES

[1] C. Ding, X. Qiu, F. Xu, X. Liang, Z. Jiao, and F. Zhang, "Synthetic aperture radar three-dimensional imaging—From TomoSAR and array InSAR to microwave vision," *J. Radars*, vol. 8, no. 6, pp. 693–709, 2019.

[2] C. Ding, X. Qiu, and Y. Wu, "Concept, system, and method of holographic synthetic aperture radar," *J. Radars*, vol. 9, no. 3, pp. 399–408, 2020.

[3] W. Hong, Y. Wang, Y. Lin, W. Tan, and Y. Wu, "Research progress on three-dimensional SAR imaging techniques," *J. Radars*, vol. 7, no. 6, pp. 633–654, 2018.

[4] Z. Jiao, C. Ding, X. Qiu, L. Zhou, L. Chen, D. Han, and J. Guo, "Urban 3D imaging using airborne TomoSAR: Contextual information-based approach in the statistical way," *ISPRS J. Photogramm. Remote Sens.*, vol. 170, pp. 127–141, Dec. 2020.

[5] P. Pasquali, C. Prati, F. Rocca, M. Seymour, J. Fortuny, E. Ohlmer, and A. Sieber, "A 3-D SAR experiment with EMSL data," in *Proc. Quant. Remote Sens. Sci. Appl. (IGARSS)*, vol. 1, 1985, pp. 784–786.

[6] G. M. del Campo, M. Nannini, and A. Reigber, "Statistical regularization for enhanced TomoSAR imaging," *IEEE J. Sel. Topics Appl. Earth Observ. Remote Sens.*, vol. 13, pp. 1567–1589, 2020.
[7] A. Reigber and A. Moreira, "First demonstration of airborne SAR tomography using multibaseline L-band data," *IEEE Trans. Geosci. Remote Sens.*, vol. 38, no. 5, pp. 2142–2152, Sep. 2000.
[8] X. X. Zhu and R. Bamler, "Very high resolution spaceborne SAR tomography in urban environment," *IEEE Trans. Geosci. Remote Sens.*, vol. 48, no. 12, pp. 4296–4308, Dec. 2010.
[9] X. X. Zhu and R. Bamler, "Tomographic SAR inversion by L_1-norm regularization—The compressive sensing approach," *IEEE Trans. Geosci. Remote Sens.*, vol. 48, no. 10, pp. 3839–3846, Oct. 2010.
[10] X. Zhu and R. Balmer, "Demonstration of super-resolution for tomographic SAR imaging in urban environment," *IEEE Trans. Geosci. Remote Sens.*, vol. 50, no. 8, pp. 3150–3157, Aug. 2012.
[11] X. Zhu and R. Balmer, "Super-resolution power and robustness of compressive sensing for spectral estimation with application to spaceborne tomographic SAR," *IEEE Trans. Geosci. Remote Sens.*, vol. 50, no. 1, pp. 247–258, Jan. 2012.
[12] A. Reigber, P. Prats, and J. J. Mallorqui, "Refined estimation of time-varying baseline errors in airborne SAR interferometry," *IEEE Geosci. Remote Sens. Lett.*, vol. 3, no. 1, pp. 145–149, Jan. 2006.
[13] N. Cao, H. Lee, E. Zaugg, R. Shrestha, W. E. Carter, C. Glennie, Z. Lu, and H. Yu, "Estimation of residual motion errors in airborne SAR interferometry based on time-domain backprojection and multisquint techniques," *IEEE Trans. Geosci. Remote Sens.*, vol. 56, no. 4, pp. 2397–2407, Apr. 2018.
[14] J. A. Tropp and A. C. Gilbert, "Signal recovery from random measurements via orthogonal matching pursuit," *IEEE Trans. Inf. Theory*, vol. 53, no. 12, pp. 4655–4666, Dec. 2007.
[15] S. S. Chen, D. L. Donoho, and M. A. Saunders, "Atomic decomposition by basis pursuit," *SIAM Rev.*, vol. 43, no. 1, pp. 129–159, Jan. 2001.
[16] I. Daubechies, M. Defrise, and C. De Mol, "An iterative thresholding algorithm for linear inverse problems with a sparsity constraint," *Commun. Pure Appl. Math.*, vol. 57, no. 11, pp. 1413–1457, Nov. 2004.
[17] A. Beck and M. Teboulle, "A fast iterative shrinkage-thresholding algorithm with application to wavelet-based image deblurring," in *Proc. IEEE Int. Conf. Acoust., Speech Signal Process.*, Apr. 2009, pp. 693–696.
[18] A. Bech, "A fast iterative shrinkage-thresholding algorithms for linear inverse problems," *SIAM J. Imag. Sci.*, vol. 2, no. 1, pp. 183–202, 2009.
[19] K. X. Zhao, H. Bi, and B. C. Zhang, "SAR tomography method based on fast iterative shrinkage-thresholding," *Syst. Eng. Electron.*, vol. 39, no. 5, pp. 1019–1023, May 2017.
[20] D. Kim and D. Park, "Element-wise adaptive thresholds for learned iterative shrinkage thresholding algorithms," *IEEE Access*, vol. 8, pp. 45874–45886, 2020.
[21] Q. Bao, Y. Lin, W. Hong, W. Shen, Y. Zhao, and X. Peng, "Holographic SAR tomography image reconstruction by combination of adaptive imaging and sparse Bayesian inference," *IEEE Geosci. Remote Sens. Lett.*, vol. 14, no. 8, pp. 1248–1252, Aug. 2017.
[22] E. Ertin, R. L. Moses, and L. C. Potter, "Interferometric methods for three-dimensional target reconstruction with multipass circular SAR," *IET Radar, Sonar Navigat.*, vol. 4, no. 3, pp. 464–473, 2010.
[23] O. Ponce, P. Prats-Iraola, R. Scheiber, A. Reigber, and A. Moreira, "First airborne demonstration of holographic SAR tomography with fully polarimetric multicircular acquisitions at L-band," *IEEE Trans. Geosci. Remote Sens.*, vol. 54, no. 10, pp. 6170–6196, Oct. 2016.
[24] J. R. Fienup and A. M. Kowalczyk, "Phase retrieval for a complex-valued object by using a low-resolution image," *J. Opt. Soc. Amer. A, Opt. Image Sci.*, vol. 7, no. 3, pp. 450–458, 1990.
[25] M. Guizar-Sicairos, S. T. Thurman, and J. R. Fienup, "Efficient subpixel image registration algorithms," *Opt. Lett.*, vol. 33, no. 2, pp. 156–158, 2008.
[26] M. A. T. Figueiredo, R. D. Nowak, and S. J. Wright, "Gradient projection for sparse reconstruction: Application to compressed sensing and other inverse problems," *IEEE J. Sel. Topics Signal Process.*, vol. 1, no. 4, pp. 586–597, Dec. 2007.
[27] I. H. Shahrezaei, M. Kazerooni, and M. Fallah, "A complex target terrain SAR raw data generation and evaluation based on inversed equalized hybrid-domain algorithm processing," *Waves Random Complex Media*, vol. 27, no. 1, pp. 47–66, Jan. 2017.

DONG HAN received the B.S. degree in automation specialty from the University of Science and Technology of China, Hefei, China, in 2017. He is currently pursuing the Ph.D. degree in signal and information processing with the University of Chinese Academy of Sciences, Beijing, China. His research interests include SAR tomography and holography.

LIANGJIANG ZHOU received the B.S. degree in electronic engineering from the University of Science and Technology of China, Hefei, China, in 2004, and the Ph.D. degree in signal and information processing from the Graduate University of the Chinese Academy of Sciences, Beijing, China, in 2009. He is currently with the National Key Laboratory of Microwave Imaging Technology, Aerospace Information Research Institute, Chinese Academy of Sciences, Beijing. His research interests include SAR system and SAR interferometry.

ZEKUN JIAO received the B.S. degree in electronic engineering from the University of Science and Technology of China, Hefei, China, in 2014, and the Ph.D. degree in signal and information processing from the University of Chinese Academy of Sciences, Beijing, China, in 2019. He is currently with the National Key Laboratory of Microwave Imaging Technology, Aerospace Information Research Institute, Chinese Academy of Sciences, Beijing. His research interests include SAR tomography and holography.

BINGNAN WANG received the Ph.D. degree in signal and information processing from the University of Chinese Academy of Sciences, Beijing, China, in 2011. He is currently an Associate Research Fellow with the National Key Laboratory of Microwave Imaging Technology, Aerospace Information Research Institute. His research interests include signal processing of advanced synthetic aperture radar systems, including theory and applications of SAR interferometry, digital array SAR signal processing, and UAV-SAR imaging and detection.

YACHAO WANG received the Ph.D. degree in photogrammetry and remote sensing from the China University of Mining and Technology, Xuzhou, China, in 2017. He is an Assistant Researcher with the Aerospace Information Research Institute, Chinese Academy of Sciences. His research interests include image registration and SAR interferometry.

YIRONG WU received the master's degree from the Beijing Institute of Technology, Beijing, China, in 1988, and the Ph.D. degree from the Institute of Electronics, Chinese Academy of Sciences (IECAS), Beijing, in 2001. Since 1988, he has been with IECAS, where he is currently the Director. He has over 30 years of experience in radar processing system design. His research interests include microwave imaging, signal and information processing, and related applications.